Electrical aging of fluoropolymer cable insulation materials induced by partial discharge

Emre Kantar [1], Katharina K Eie-Klusmeier[1], Torbjørn Andersen Ve[1], Marit-Helen Ese[1], and Sverre Hvidsten[1]

[1]SINTEF Energi AS

March 18, 2024

Electrical aging of fluoropolymer cable insulation materials induced by partial discharge

Emre Kantar, Katharina K. Eie-Klusmeier, Torbjørn Andersen Ve, Marit-Helen Ese, and Sverre Hvidsten

Abstract—**This study investigates AC electrical aging induced by partial discharge (PD) in fluoropolymer cable insulation materials, namely fluorinated ethylene propylene (FEP) and perfluoroalkoxy (PFA), with the cross-linked polyethylene (XLPE) serving as the reference material. Utilizing a specialized electrical aging setup and comprehensive surface characterization techniques, we compared the aging behavior of FEP and PFA to that of XLPE under identical electrical discharge conditions. Over a three-week aging process, the stability of phase-resolved partial discharge (PRPD) patterns for FEP and PFA suggested minimal changes in surface chemistry and roughness, unlike XLPE. FTIR and Raman spectroscopy results confirmed minimal changes in the surface chemistry of FEP and PFA, while microscopic and profilometric analyses demonstrated notably fewer PD-induced alterations on their surfaces. These findings suggest a gradual aging effect on the electrical insulating properties of fluoropolymers, likely due to their resilient carbon-fluorine bonds, contrasting with the immediate and significant erosion and by-product formation observed in XLPE upon PD exposure.**

Index Terms—**Aging, cable insulation, FEP, fluoropolymers, partial discharge, PFA, XLPE.**

I. INTRODUCTION

TODAY'S electrical power cable insulation systems predominantly utilize cross-linked polyethylene (XLPE) and ethylene propylene rubbers (EPR). These polymers, enhanced through years of dedicated service, advancements, and rigorous research, demonstrate prolonged durability. This is attributed to their outstanding processability, ease of operation, remarkable dielectric characteristics, and cost-effectiveness in maintenance across diverse conditions [1], [2]. Nonetheless, their use is limited by the maximum continuous service temperature of 90°C, emphasizing the need to incorporate alternative extrudable materials capable of withstanding higher temperatures into the design. Viable substitutes include extrudable fluoropolymers, which have already found applications in several high-temperature settings [3]–[7].

The cable insulation, terminations, and joints of high-voltage power cable systems are critical sections prone to partial discharges (PDs). The PD phenomenon has been a major research focus over the past half-century, particularly for

materials such as XLPE and EPR. During the manufacturing, transportation, or assembly processes of power cables, defects capable of triggering PDs at service voltage levels may be introduced. Additionally, mechanical stresses, thermal stresses, and environmental stresses can lead to oxidation and chemical decomposition and affect the development of water and electrical trees as well as space charge accumulation in the insulation [8]. Moreover, different defect types have varying aging stages and propagation speeds within the insulation, which can be identified by analyzing PD patterns [9]. Therefore, understanding how insulation materials age in the presence of PDs is crucial to the development of insulation systems.

Fluoropolymers, such as polyvinylidene fluoride (PVDF), perfluoro alkoxy (PFA), fluorinated ethylene propylene (FEP), and ethylene tetrafluoroethylene copolymer (ETFE), have been recognized for their excellent electrical insulating properties. They are often utilized as insulating materials in low-voltage aviation cables because of their resistance to high temperatures, corrosion, and aging [10]. Their chemical structure is predominantly made up of carbon-fluorine backbones (C−F), which are known for their high bond dissociation energy and low polarity [11], ensuring high chemical stability, which is integral to their electrical insulating capabilities [11], [12]. Their applications extend to various fields due to their outstanding mechanical and chemical resistance, along with their high transparency [5]. Like other polymers, fluoropolymers also age under various environmental and operational conditions. Exposure to electrical stress or radiation can alter their molecular structure [13].

Until recently, literature on the fundamental dielectric phenomena in fluoropolymers for high-voltage cable applications was scarce. Only a series of articles has emerged focusing on DC cable applications, including space charge, conduction, partial discharge at DC voltage, and degradation during arcing [14]–[16]. While PD-induced aging phenomena in XLPE are well documented (see e.g., [17]–[20]), PD-aging in fluoropolymers has not received much attention in the literature. The main purpose of this work has been to investigate AC electrical aging induced by PD in two fluoropolymers, FEP and PFA, using a dedicated electrical aging setup and various surface characterization techniques. Due to its well-documented aging characteristics, XLPE was used as a reference material.

II. AGING OF POLYMERIC INSULATION

A. Electrical (PD-induced) Aging of Polymeric Insulation

Electrical discharges (PD) release energy as current pulses, heat, light, and sound. Dielectric degradation due to PD arises mainly from ultraviolet radiation, chemical degradation caused

by dissociation products, physical surface damage by hot electron and particle bombardment, particularly nitrogen ions, and the production of high-energy gases causing localized heating, melting, and deterioration [21]. The interplay between PD within a cavity and its surrounding dielectric material is intricate. As the dielectric undergoes aging due to PD, this aging process, in turn, influences the behavior of the PD mechanism itself [17]–[19].

In XLPE, the primary components are long-chain hydrocarbons. These hydrocarbons are largely nonpolar, which is partly why they are good insulators. When XLPE is exposed to electrical discharges, reactive oxygen species (ROS) such as ozone (O_3), hydroxyl radicals (OH), and superoxide radicals (O_2^-) can form. These ROS can oxidize the hydrocarbon chains in XLPE, leading to the introduction of polar functional groups like carbonyl groups (C=O) and ketones [22]. The presence of these polar entities compromises the material's insulating properties by altering its dielectric constant, making it more chemically reactive and thus weakening the mechanical and electrical breakdown strength of XLPE [21].

Similar to hydrocarbon polymers, the electrical aging of fluoropolymers is a complex interaction of their molecular structure, environmental conditions, and operational stressors. Both FEP and PFA display similar electrical properties, such as their dielectric constants, which are 1.9 for FEP and 2.1 for PFA. Both materials have an identical dielectric strength of 22 kV/mm and share an electrical resistivity of $10^{16}\,\Omega \cdot m$ [23]. The inherent chemical stability provided by the C−F bonds in these polymers makes them intrinsically resistant to electrical aging [24]. For instance, FEP is reported to resist oxidation under solely thermal aging stress at temperatures as high as 140 °C [25]. However, over prolonged exposure to electrical stresses, especially at high voltages, even these robust bonds can deteriorate. The degradation mechanisms in fluoropolymers, such as PFA and FEP, under electrical stress often involve the slow breakdown of C−F bonds, leading to the formation of carbon-centered radicals [26]. These radicals may react with trace impurities or degrade further, forming defects in the polymer matrix. Over time, accumulated defects alter the material's dielectric properties and reduce its insulating capability [26].

However, the literature still lacks in-depth research on how PD-induced aging affects the insulating properties of fluoropolymers, influencing their mechanical and electrical breakdown strength.

B. Degradation Mechanisms

Research on PD degradation mechanisms has predominantly concentrated on XLPE (and its derivatives), EPR, and epoxy. Consequently, the mechanisms detailed herein pertain to the PD-induced aging of these materials.

Considering a flat cavity or an air gap between dielectric surfaces containing hydrogen, carbon, and oxygen (either in gas or solid form), the aging process generally follows the five steps shown in Fig. 1 [18]. The surface conductivity of the cavity rises because of chemical reactions due to humidity and dissociation products of air. Increased surface conductivity

is observed shortly after PD initiation [17], [18], [20], and often, liquid formations are seen on the cavity surface. As the aging duration is prolonged, oxygen is regenerated faster than it is consumed, which likely keeps increasing the surface conductivity. In addition to oxygen, gaseous by-products such as CO and CO_2 are generated [27]. Dissociation of CO and CO_2 also releases more oxygen [27]. This causes oxidation of the polymer, and during the polymer oxidation, the polymer typically undergoes chemical structure alteration with the formation of oxygen-containing groups and experiences changes such as cross-linking, chain scission, thermal degradation, discoloration, reduced mechanical properties, altered electrical properties, surface property changes, and potential for environmental stress cracking [21], [25]. The surface texture grows rougher not only due to oxidation but also from the impact of charge carrier bombardment and the accumulation of PD by-products. Continuous PD results in the formation of solid by-products like crystals, recognized as hydrated oxalic acid [28]. Field amplification at crystal points can intensify PDs, resulting in the formation of pits and the initiation of tree growth. Ultimately, this growth can cause an electrical breakdown. In the presence of fillers within the dielectric, the insulation around these particles is the most susceptible to degradation [17].

In our study, XLPE, FEP, and PFA will be subjected to PD aging. The aging mechanisms observed in the FEP and PFA samples are compared with those of XLPE from both our experimental findings and existing literature for XLPE.
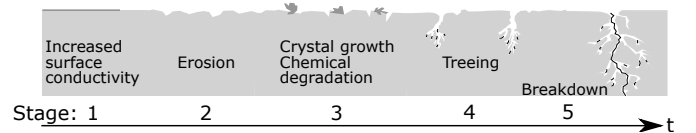

Fig. 1. Stages of surface degradation due to PD. Readapted from Temmen [18].

III. EXPERIMENTAL METHODS AND MATERIALS

This section presents the materials, experimental setup, and material characterization techniques applied to the samples.

A. Materials and Sample Casting

The experimental setup includes a rod-plane configuration to initiate PDs in an air gap between two polymer samples, as indicated in Fig. 2. Cylindrical discs, each 1 mm thick and 100 mm in diameter, were cast from FEP, PFA, and XLPE materials. Table I presents the casting parameters used for each material. FEP was cast in two steps, from pellets to small discs and then to discs of the specified dimensions. PFA was delivered as thin tapes from the manufacturer and cast directly into the correct sample dimension. As the processing of fluoropolymers presents the potential release of toxic fumes [29], health and safety measures were established and used during casting. To make XLPE samples, polyethylene (PE) pellets were initially extruded into thick tapes, which were subsequently cross-linked during the casting process to produce discs with the desired dimensions. After casting, samples for each material were preconditioned in a separate vacuum chamber for a week at 70 °C.

TABLE I

TEMPERATURE, TIME, AND PRESSURE SETTINGS FOR THE
COMPRESSION MOLDING OF THE POLYMER SAMPLES.

	XLPE	FEP	PFA
Low pressure	120 °C 10 min (2.9 MPa)	290 °C* 30 min (1.8 MPa)	328 °C* 30 min (0 MPa)
High pressure	170 °C 30 min (18 MPa)	260 °C 2 min (7.2 MPa)	308 °C 2 min (7.2 MPa)

* Temperature was set to high-pressure temperature as samples were inserted to give an initial temperature gradient.

B. Experimental Setup

Fig. 2 illustrates the axisymmetric cross-section of the aging setup. A cylindrical, disc-shaped, air-filled cavity, 2 mm in height and 15 mm in radius, was formed between two polymer samples using a spacer. This spacer, made of the same polymer as the top and bottom samples, ensures that the entire disc-shaped cavity, including its walls, consists solely of the same material. The exposed surfaces of the samples will then be aged by discharges during the experiments. To avoid compression of the cavity, a metal spacer was placed around the polymer spacer. The cavity was positioned between two electrodes, a ground plane disc electrode at the bottom and an HV electrode on top. The HV electrode was cast in epoxy under 15 bar nitrogen pressure to prevent any discharges from occurring in voids present in the bulk of the material. The bottom sample was cast directly onto the ground electrode, while the top sample was glued to the HV electrode after casting, using an instant adhesive gel. All the metals in the setup were made from Hastelloy, a nickel alloy characterized by its high-temperature endurance and exceptional corrosion resistance, not corroding when in contact with fluoropolymers [30]. As there is a chance of generating hazardous gases during the aging of fluoropolymers [29], a plexiglass hollow cylinder with a connected evacuation tube was placed around the setup to remove any gases leaking from it.
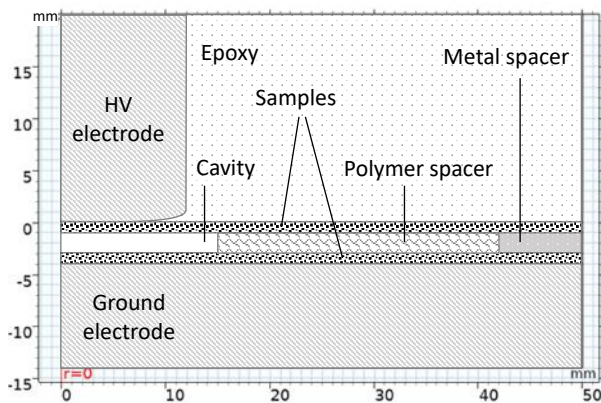

Fig. 2. Diagram depicting the axisymmetric cross-sectional view of the experimental setup for PD aging.

Fig. 3 presents the schematic diagram of the PD measurement circuit used in the experiments. The 'test object' corresponds to the setup described in Fig. 2. A 100-kV PD-

free transformer was used coupled with a noise-free signal generator (50 Hz AC). A 30 MΩ HV resistor was connected in series with the test object to protect the electrical equipment. The PD measurement system is connected in series with a coupling capacitor of 800 pF. Both the PD unit and the capacitor are paralleled to the test object, which has a capacitance of approximately 3.2 pF. For data acquisition, the PD measurement system is linked to a computer via an optical fiber cable. A three-week aging duration was chosen at 50 Hz AC voltage at 15 kVrms based on the initial experiments.
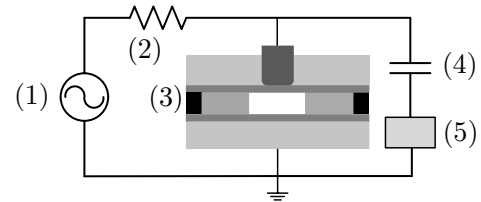

Fig. 3. Experimental setup for PD aging. (1) High voltage AC source. (2) Current limiting resistor. (3) Test object (sample and the electrode system). (4) Coupling capacitor. (5) PD measurement system.

A commercial PD acquisition unit was used for collecting PD data during aging. Preliminary testing of the system indicated that noise levels were detected at approximately 5 pC at 15 kVrms with some sporadic peaks of 7–8 pC magnitude. The PD threshold was, therefore, set to 10 pC to ensure that all the registered PD originated from the air gap. However, the contribution of smaller pulses (< 10 pC) was not taken into account. More explanation for the possible effects of this will be given in the Discussion section. The measurement system was calibrated according to IEC 60270 before each aging experiment.

Two types of data were collected during the aging experiments. First, the following parameters about the voltage and PD were saved to a trend file every 900 ms: RMS value of the voltage input (V), the PD level (the apparent charge as defined in IEC 60270), and the number of PD events detected per second. Secondly, stream files containing each PD event were recorded for five minutes each hour. From this data, the discharge magnitude (Q_a), number of discharges (n), voltage phase (ϕ), and grid voltage (V) data could be exported to MATLAB-compatible files. Numeric (deterministic) PD parameters, such as the number of the PD pulses, average and maximum discharge magnitude (99th percentile employed to eliminate outliers), and discharge energy, were extracted using the exported PD data.

C. Electric Field Distribution Simulations

The electric field distribution in the setup was calculated using a FEM software. An axisymmetric FEM simulation calculation, as illustrated in Fig. 2, was performed at 15 kVrms AC voltage at the HV electrode while the rest of the metallic parts were kept at the ground potential. The 'extremely fine' mesh option was used to calculate the field as accurately at the interfaces as possible.

The electric field strengths at critical interfaces, such as the triple point where epoxy, Hastelloy, and the polymer sample

meet, as well as the interfaces between each sample and the air gap, were evaluated.

D. Surface Characterization

Different characterization methods were used to evaluate the degradation of the polymers after three weeks of aging. The samples were first examined using a microscope and a non-contact optical profilometer. From the profilometry scans, the mean surface roughness was calculated by a weighted average of three scans of each sample at different positions. Each scan measures 2.3×1.7 mm and was weighted according to the percentage of data points in the scan. If crystals are detected on the aged surfaces, all data above a certain height where crystals were detected was removed to prevent them from dominating the calculations for the aged surfaces.

Afterward, smaller samples (10 mm in diameter) were punched out from the aged polymer top and bottom samples at three different sections (pos.): i. Pos. 1: the actively aged area (cavity), ii. Pos. 2: the interface between the cavity and underneath the polymer spacer, and iii. Pos. 3: underneath the metal spacer. In total, nine samples were punched out from each polymer sample, as illustrated in Fig. 4. Each set of samples was then used for the characterization with FTIR and Raman. One set of samples was stored as a backup for potential future characterization using another technique, if necessary. For comparison, equivalent samples were also punched out from unaged samples. A 670/620 FTIR Imaging Microscope equipped with a 64×64 focal plane array (FPA) detector was used in transmission mode to investigate the chemical composition of both unaged and aged surfaces in various depths from the surface into the bulk of the material. For FTIR characterization, the punched-out samples were initially divided into two half disks. Subsequently, 250-μm-thick slices were cut from the vertical cross-section of one of the half disks at four various depths, moving from the aged surface into the bulk for each sample, as illustrated in Fig. 4. Characterization was performed at six different radial positions for each slice. One measurement was set to average over 16 scans in the range 4000 cm^{-1} to 400 cm^{-1}, with a resolution of 4 cm^{-1}.
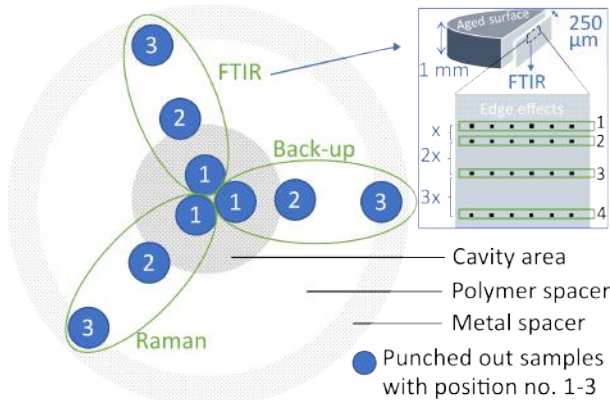

Fig. 4. Sampling of positions 1–3 from the aged samples.

Raman spectroscopy was performed on the aged surfaces of the samples to complement the FTIR measurements, aiming to explore the chemical composition of any crystals or other by-products. The measurements were performed using the WITec Alpha 300R system with a 532 nm green laser. A laser power of 5 mW and 7.5 mW were used to reduce fluorescence interference in the data. Each spectrum was obtained using six accumulations with a 10 s integration time. All spectra underwent data processing to eliminate fluorescence and background interference from the bulk material.

IV. RESULTS AND DISCUSSION

For the experimental analysis, we aged several samples of each material to replicate the effects of PD-induced electrical aging. After aging, we evaluated these samples to discern those that most accurately demonstrated the typical aging behaviors of each material. Thus, the results discussed herein reflect the general response of each material to electrical aging.

A. Electric Field Simulation

The electric field distribution in critical sections of the axisymmetric setup, shown in Fig. 5, employs a jet colormap. Fields below 2.6 kV/mm—-the threshold for electron avalanches, i.e., discharges [31]-——are omitted to accentuate areas of higher field strength. Notably, the highest field, around 7.2 kV/mm, concentrates inside the cavity. Fields at interfacial surfaces, such as the HV electrode's curvy edge, epoxy encase, cavity wall, and the top and bottom samples, slightly exceed 2.6 kV/mm. It is important to note that the theoretical PD inception voltage (PDIV) for the 2 mm cylindrical cavity, calculated to be 4.1 kV/mm at 1 bar and 20 °C based on a detailed discharge model [32], is closely aligned with the observed PDIVs, ranging from 7.9 to 8.3 kV.

The tangential field distribution at the critical interfaces is plotted in Fig. 6, with a focus on interfaces at the top sample and the air gap, the bottom sample and the air gap, and at the triple point where the epoxy, HV electrode (Hastelloy), and the top sample intersect. Each field line shown corresponds to the distribution along the line depicted in the same color below. Additionally, field distribution at the void surfaces normal to the electrical field at the cavity wall, measured 0.1 mm inside of the polymer spacer, is depicted at the inlet of Fig. 6. The highest value is noted at the edge of the wall (at 1 mm), about 4 kV/mm, an edge effect due to high field strength at different permittivities near the HV electrode. It indicates that the field strength exceeds 2.6 kV/mm, suggesting that discharges can occur at the cavity walls.

B. PD aging

Three different types of plots displaying the discharge activity are shown in this section. Trend plots, phase-resolved PD (PRPD) plots and some PD parameters using the extracted data (ϕ, Q_a, V) are presented.

1) Trend plots: Figs. 7a–7c show the trend plots for the aging of XLPE, FEP, and PFA, respectively. The blue dotted line represents the average value of the registered discharges every 900 ms, and the dashed black line shows the moving average (with a window size of 500 data points) of these
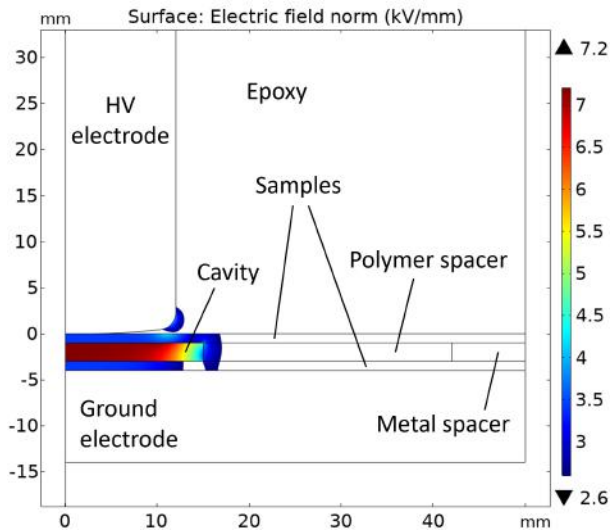
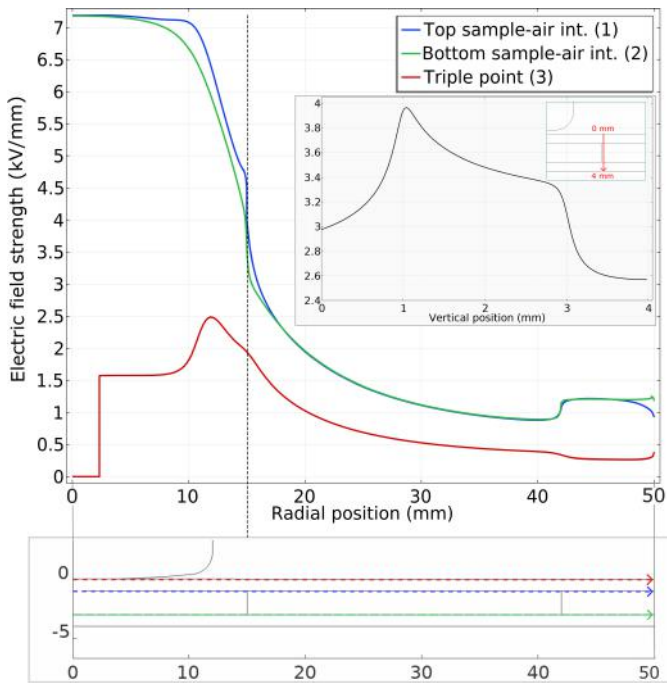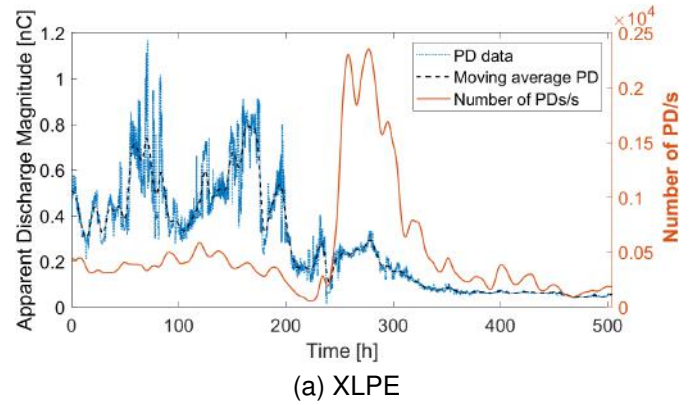Fig. 5. Electric field distribution in the setup.

Fig. 6. Variation of electric field strength as a function of radial position at critical interfaces. The vertical dashed line represents the boundary delineated by the cavity wall.

(a) XLPE

(b) FEP

(c) PFA

Fig. 7. The trend plots display the apparent discharge magnitudes (raw and moving average data) and number of PDs over three weeks as functions of time at 15 kVrms. (a) XLPE. (b) FEP. (c) PFA.
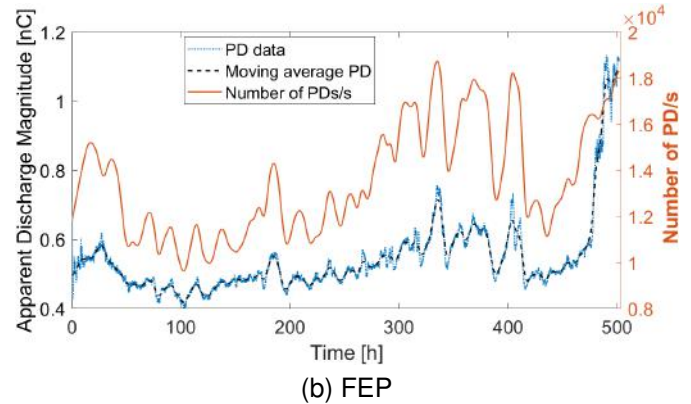
values. The red line shows the number of PDs per second (PDs/s) at the given PD magnitude.

In the case of XLPE in Fig. 7a, the PD magnitude was oscillating between 200–1200 pC in the first 200 h, after which a declining trend was observed, and the PD magnitude settled around 50 pC. The number of PDs/s significantly increased after 240 h, and this increased activity lasted around 100 h. At the end of the aging, both the PD data and PDs/s settled down to their lowest magnitudes of 45 pC and 190, respectively.
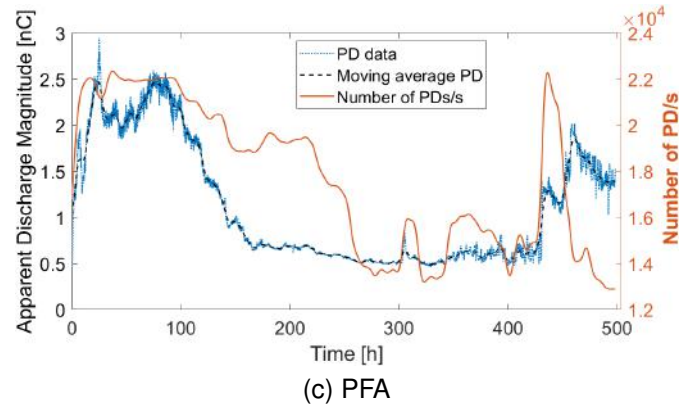
A similar trend was observed for the PFA sample in Fig. 7c, where there were PDs with magnitudes as high as 3000 pC. The declining trend started earlier in the PFA than it did for XLPE, after about 100 h, and settled around 500 pC. The PD magnitude remained stable until 425 h, after which there

was a relative increase up to 2000 pC. The number of PDs/s followed the PD magnitude pattern with some lag.

Unlike the XLPE and PFA, there was not a declining PD trend in the case of FEP, where the PD magnitude remained stable around 500 pC until the last 24 h, after which it more than doubled, as shown in Fig. 7b. The number of PDs/s followed the PD data quite accurately during the entire aging period. These trend plots will be benchmarked with PRPD plots in the next section, and possible mechanisms will discussed.

2) PRPD plots: PRPD plots of each sample represent the PD events taking place in the entire 5-minute duration. These data were analyzed, and the evolution of the PD patterns was evaluated. The representative patterns before aging (0 h), at 10 days (360 h), and at the end of the aging (504 h) are shown in Figs. 8a–8i for each material. The surfaces of the

top and bottom samples were subjected to approximately the same field strength, as verified by the field lines in Fig. 6. The small variation occurs because of the different diameters of the metallic electrodes.

Referring to Figs. 8a–8c for XLPE from 0 h to 504 h, the PD clusters became significantly fewer and narrower. There were fewer PD events observed during the positive voltage cycle compared to the negative cycle. The increased availability of electrons from the bottom electrode, owing to its larger surface area following the voltage polarity reversal, might have facilitated the formation of more electron avalanches, as suggested in [33]. During the negative cycle, the maximum PD magnitude appears to exceed that of the positive cycle. This could be due to an enhanced electric field along the electron avalanche pathway in the air gap, which may allow some avalanches to extend farther, leading to a greater PD charge magnitude [33].

The PD inception voltage is influenced by both the external field applied and the field generated by surface charges left from preceding PD events [17]. There are several consequences of increased surface conductivity (Stage 1 in Fig. 1). First, it causes the spread of charges from previous PDs over a larger area, reducing the local field these charges generate. This results in a quicker recovery of the electric field within the cavity, enabling it to discharge again. Second, this increased conductivity provides a source of potential initiation electrons held in shallow traps. Third, if the cavity walls become highly conductive, they may prevent the accumulation of a sufficiently strong internal field, quenching cavity discharges. This decrease in the statistical time lag for the initiation electron's release implies that PDs can commence immediately when the external field surpasses the minimum inception field, thereby contracting the PD phase pattern/distribution [17].

Additionally, enhanced surface conductivity inhibits the formation of simultaneous PD locations [17], [18]. The PRPD patterns shown in Figs. 8a–8c exhibit this behavior. In Stage 2 in Fig. 1, crystal formation can occur, with PDs igniting at the tips of any crystals. Consequently, field enhancement at the crystal tips leads to a lower local PDIV, yet the PD magnitude stays minimal, owing to the confined size of the affected area. Surface characterization results in Section IV-C will reveal if it was the case for the XLPE.

In the case of FEP, different patterns were observed. As can be seen in Fig. 8f, in the final hours, a shift in the PD pattern was noted, transitioning from a turtle-like to a rabbit-like appearance. PD clusters did not become narrower or fewer than for XLPE. Similar Q_a was observed throughout the aging except for the rabbit-like clusters. On the contrary, the PD density increased significantly, as shown by the color bars in Figs. 8d–8f. The trend plot depicted in Fig. 7b also captured this significantly increased PD activity. Similar trends were also observed for the PFA.

As mentioned in Section II-A, while the cavity surface undergoes aging due to PDs, its physical and chemical characteristics are altered, which in turn influences the PD patterns. Micro-cracks and crystal formation, resulting from changes in chemical composition (such as oxidation or the creation of new functional groups), might explain the intensified and/or locally enhanced PD activity and the alterations in the PRPD distributions. The accumulation of space charges in the polymer material over time can significantly distort the local electric field, leading to the formation of more branched, rabbit-like discharge patterns. This effect becomes increasingly pronounced as the polymer ages, altering its ability to trap and release charges [17].

In [34], a study on the aging process of cavities within the solid insulation of power cables was conducted, dividing the process into three distinct phases. During the initial phase, the onset of streamer discharge causes the decomposition of gas trapped within the cavity. This leads to a decrease in the pressure of the gas contained and an increase in the conductivity of both the gas and the cavity surface. These findings, illustrated as Stage 1 in Fig. 1, are in agreement with those of many researchers, such as [20], [27], [35]–[39].

In a high electric field with elevated local temperatures, the breaking of the strong C−F bonds of FEP and PFA might lead to partial oxidation processes (as explained in Section II-B) [25]. This could potentially result in the formation of CO and CO_2. The shift from a turtle-like pattern to a rabbit-like form could then be caused by the increase in the concentration of CO and CO_2, which are electronegative gases and can absorb free electrons that would otherwise contribute to the discharges [34], [40]. Therefore, as the time gap between consecutive discharges extends, PD is initiated at higher voltage levels, consequently elevating the PD charge value [40]. Typically, these substantial PD events emerge close to the voltage zero crossing point within each half cycle, resulting in the formation of a rabbit-like pattern [27], [38].

Another mechanism can be linked to varying rates of charge de-trapping from surfaces that are negatively and positively charged [41]. Specifically, the initial discharge following a reversal in voltage polarity is triggered by the release of free electrons from the surface that is negatively charged. Meanwhile, the free electrons for subsequent pulses within the same half cycle originate from the surface that is positively charged [40], [41]. Electrons are emitted from negatively charged surfaces at a slower rate than from positively charged surfaces. This results in a higher discharge intensity for the first pulse compared to subsequent ones, a phenomenon that manifests as the so-called slow component in the PD pulse.

Several hours following the application of voltage, a transition to a rabbit-like PD pattern from a turtle-like one was noted in [42]. In their study, they aged polyethylene (PE) samples using an experimental rig that was based on the CIGRE Method II, which is akin to the setup utilized in this work. In a rabbit-like pattern, as described above, the initial PD pulse after the polarity reversal tends to be larger than its successors and may be separated into fast and slow components in the time domain. They argued that the fast component's time constant is primarily linked to streamer development, whereas the slow component results from the migration of residual charges on the insulating surface, which reflects the effective surface conductivity in PD-induced aging. They further investigated the impact of charge migration across the cavity surface by studying a similar cylindrical air gap with and without metal surfaces (only on one surface and
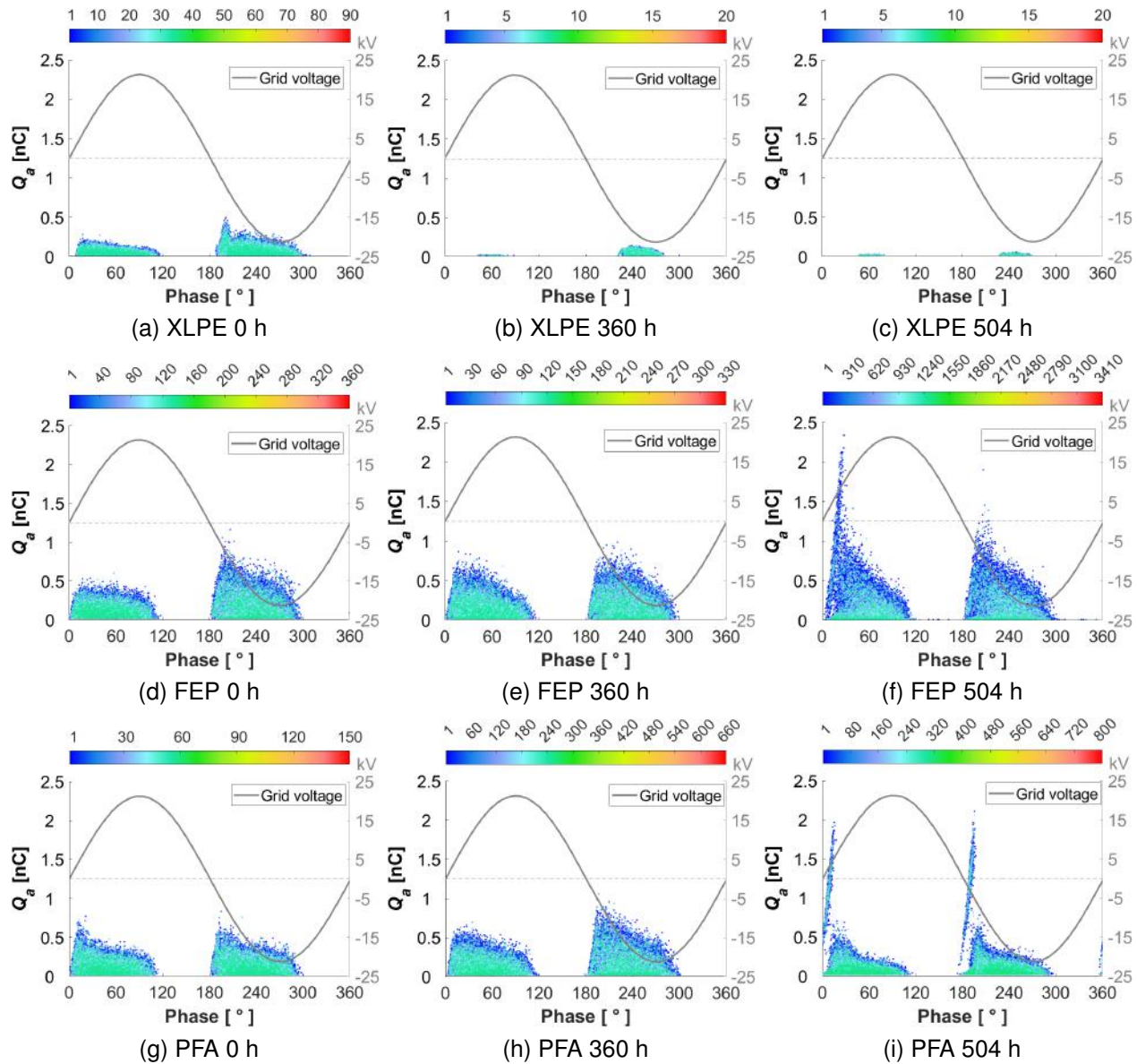
Fig. 8. PRPD plots from the aging of XLPE, FEP, and PFA. Each registered discharge is plotted as a point and color bars show concentrations of PDs. The apparent discharge magnitude is indicated on the left axis, while the voltage is plotted on the right y-axis. The number of hours of aging is indicated below each plot.

both surfaces). Their findings revealed that in the scenario of a cylindrical cavity with metallic surfaces on both ends, the slow component was absent, while it reappeared when one of the surfaces was insulating. Therefore, the movement of residual charges on the insulating surface was believed to govern the rabbit-like pattern formation. The change in surface conductivity as a result of aging can be considered the key driver for the pattern transition from turtle-like to rabbit-like. These findings have been verified by other studies [43], [44]. In [44], it was experimentally shown in the case of electrode-bound cavities (EBC) that the surface charge can move readily into the electrode and decay more intensely than for a dielectric-bound cavity because charge can be absorbed by the electrode [43], [44].

As illustrated in Fig. 1 in a later stage of aging in the cavity, transitioning from streamer-like large amplitude pulse PDs to glow discharges with lower amplitudes can be observed due

to the changes in the electric field distribution, induced by the increased surface conductivity, humidity, and temperature [35], [45], [46]. At this stage, both the magnitude and intensity of PD pulses decline swiftly, occasionally dropping beneath the sensitivity/threshold level for PD detection, only to reappear after several hours [38]. This behavior was observed in the case of XLPE but not for FEP and PFA in Fig. 8. Despite being exposed to the same electric field for the same duration, PD magnitudes and numbers in the cases of FEP and PFA did not start to decrease during the entire aging period. As mentioned above, the reason could be that oxygen and other electronegative gases were not consumed entirely, which may be due to the still active regeneration of such reactive species. It is also reported that a rabbit-like pattern persists until the cavity surface undergoes substantial degradation or erosion [44]. This could suggest that the FEP and PFA surfaces did not undergo significant erosion by the time the aging experiments

were finalized after 504 h.

Further exploration of how residual space and surface charges, along with changes in surface conditions, contribute to PD propagation is needed. Hence, the surface characterization findings in the following section are essential to corroborate the previously discussed hypotheses.

3) PD parameters as functions of time: The number of the PD pulses, maximum and average PD magnitude, and PD energy are shown in Figs. 9a–9d. In the case of XLPE, relatively large maximum PD magnitudes were observed in the beginning, but they rapidly decreased in the first few hours and settled around 40–50 pC, as previously discussed with the PRPD plots. Higher PD activity (more PDs with higher discharge energy and PD magnitude) was observed between 140–240 h, as can be seen in the plots Figs. 9a–9d, which is also observed in the trend plot Fig. 7a. The research conducted in [38] and [27] on the aging of LDPE and PE, respectively, revealed that the gas volume initially declined rapidly to approximately 75–80% before rising to about 82–95% after 10–30 minutes, followed by a slow and steady decrease thereafter. Although the cavity we studied was not fully sealed, we can still discuss our observations regarding the generation and consumption of oxygen and electronegative gases and their effects on the PD parameters. The relatively large discharges observed initially for XLPE in Figs. 7–9 could have led to a reduction in oxygen concentration, influencing the inception time or the time lag of PD, as oxygen molecules capture free electrons [27], [38], [39], [44]. The average PD magnitude for XLPE indicates a decreasing trend (shown by the dashed line in Fig. 9c, agreeing with this hypothesis.

On the other hand, the average PD magnitude did not show a considerable change in the entire period for FEP and PFA (Fig. 9c). Similar trends to those noted for XLPE were observed only in the final few days. Trend plots in Figs. 7b–7c also suggest that a significant change for FEP occurred at the final 24 h of the experiment while it started at the final 100 h for PFA. The observed increases in the number of PDs, maximum PD magnitude, and PD energy in the final part signify that the majority of the discharges were of low magnitude, which did not affect the average PD magnitude significantly. Lastly, the discharge energy levels, PD magnitudes, and number of PDs are significantly higher for FEP and PFA than for XLPE. The average discharge energy for XLPE (0.6 mW/s) is around one-tenth of those for FEP (5.8 mW/s) and PFA (6.7 mW/s), as can be seen in Fig. 9d. These suggest that the discharges were governed by different mechanisms or that the aging stages of the cavity surfaces were different in the case of fluoropolymers, as discussed above. It is likely that the chemical and physical characteristics of FEP and PFA during the aging were different than those of XLPE, affecting the PRPD patterns and PD parameters.

C. Surface Characterization

After three weeks of aging, the polymer samples were examined using a profilometer, FTIR, Raman spectroscopy, and a light microscope. The results are presented in the following sections.
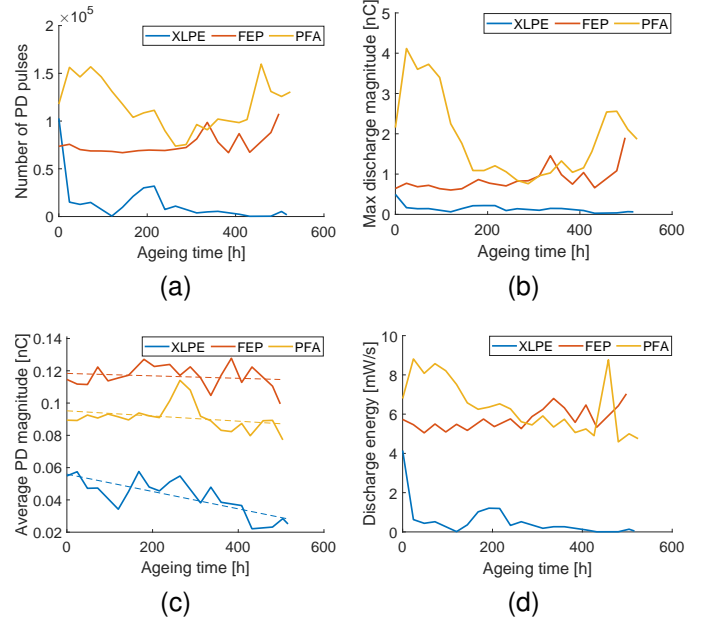

Fig. 9.   PD parameters: number of the PD pulses, maximum and average discharge magnitude, and discharge energy.

Fig. 10 displays the image of an aged XLPE top sample. The cavity area, approximately 30 mm, is easily distinguishable due to significant erosion, highlighted by a discolored region. The top right inlet image, taken using a digital microscope, reveals noticeable pitting marks and crystals. In contrast, the area where the cavity wall meets the polymer spacer (bottom right inlet image) shows fewer and less dense pitting marks, less erosion, and only a few crystals. The unaged region beneath the polymer and metal spacers exhibits no signs of pitting, erosion, or crystal formation. Similar patterns were observed in FEP and PFA samples, although the discolored areas were less evident. For the sake of brevity, only the XLPE sample is illustrated here.
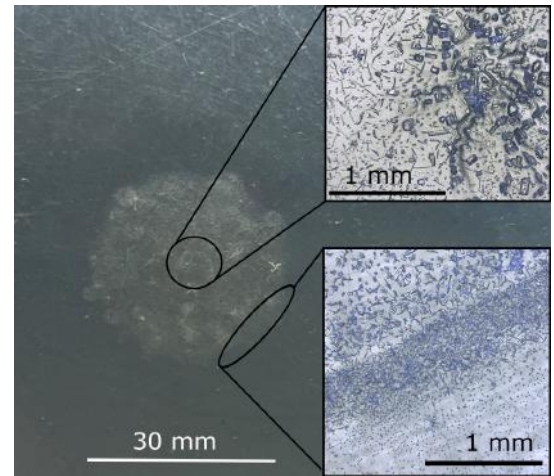

Fig. 10.   Aged cavity area of an XLPE top sample.

1) Profilometry: Table II shows the calculated mean surface roughness of Pos. 1 to 3 as shown in Fig. 4. For all the materials, calculations at Pos. 3 did not show any differences from calculations of unaged samples; thus, samples from Pos.

3 can be considered references. Calculations presented in Table II indicate that XLPE and FEP exhibit greater surface roughness at Pos. 1 compared to Pos. 3. In contrast, the surface roughness values for PFA at Pos. 1 and 3 are somewhat similar. Furthermore, for the fluoropolymers, the surface roughness at Pos. 2 is found to be less than that at Pos. 3.

The results for XLPE and FEP show that there is an increase in the measured mean surface roughness for the aged center (Pos. 1). These types of calculations cannot distinguish between the presence of peaks, for example, crystal growth, or the presence of valleys, for example, pitting. A digital filter in the software was employed to remove the crystals from the XLPE surface before the calculations. However, there is a possibility that smaller crystals were still part of the data set used, which could have led to higher roughness calculations. Additionally, abrupt steps in height, such as at the edge of a crystal, are difficult to scan and could have led to a lack of data at the crystal edges.

The PFA results do not seem to show an increase in surface roughness for Pos. 1 compared to Pos. 3. However, Pos. 1 for PFA proved difficult to scan. Generally, for the edges and unaged samples, the percentage of data points measured was well above 90%. For the aged PFA center, it dropped to as low as 40%. There is a possibility that only the data points at similar heights were registered, making the surface appear less rough than it really is. The markings from the casting molds special to PFA could have caused this problem. With some PFA samples, there seemed to be small dents remaining from the casting process. Such dents would influence the surface roughness calculations. Furthermore, the mean surface roughness calculations performed do not distinguish between different types of height differences on a surface. If there are elements of curvature or waviness on the surface, these will be included in the calculations unless they are filtered away.

Since the samples taken from Pos. 2 are at the edge of the cavity, it is anticipated that the surface roughness appears somewhere between the aged center at Pos. 1 and the unaged edge at Pos. 3. For XLPE, this is the case. The calculated surface roughness combines both aged and unaged areas. However, for both fluoropolymers, Pos. 2 has a lower surface roughness than Pos. 3. One possible explanation is that there is waviness and markings on the surface from the casting molds causing variations over a few hundred nm at different positions in a region with the same level of aging.

Fig. 11 presents representative 2D profiles of the unaged and aged surfaces. The variations in the surface of the 2D profiles are in agreement with the roughness data in Table II.
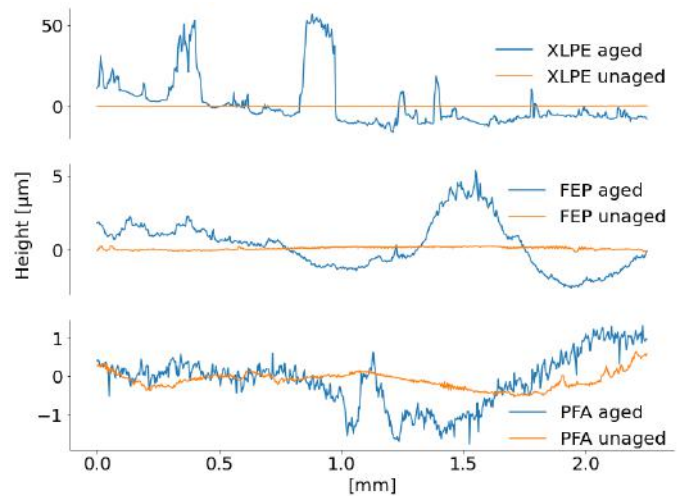

Fig. 11. 2D profiles of aged and unaged samples. Different height scales are used to feature the roughness profiles clearly.

The unaged surfaces look roughly the same, but variations can be seen more clearly for the PFA sample due to the different scaling of the height axis. Aged XLPE has the largest variations in height, and the profile covers several crystals, where the largest has a height close to 50 µm.

The first row in Table III shows 3D images generated from the profilometry data for XLPE, FEP, and PFA, respectively. In all images, the aged center appears rougher than the unaged surface. There are lines shown on the unaged surfaces that resulted from the molds used during casting. These lines are no longer visible for the aged surfaces, further indicating that aging has caused alterations to the surfaces. The application of filters, such as a data restore filter for interpolating missing data points to the raw data sets, results in images that provide a representational view of 3D profiles. Looking at actual images of the surface through microscopy is, therefore, also important.

Images of the center of the aged XLPE sample are shown in Table III at the second row. Crystals were observed on the surface after aging, which is expected based on the PD-aging mechanisms introduced in Sections II-B and IV-B. Both the size and concentration of the crystals appeared to decrease with radial distance from the center of the sample. Furthermore, the surface beneath the crystals appeared more uneven at the center than around the crystals further from the center.

The FEP surface at the center appeared to have bumps on the surface, making the surface more uneven than before aging. There were also small spots that appeared like crystals, as shown in Table III. However, comparing the crystals on the FEP to those on XLPE, they are much smaller than the ones on the XLPE sample. Whereas the crystals and erosion of the XLPE surface appear to be evenly distributed at the center of the sample, for FEP, there appear to be clusters of small crystals, as seen in Table III.

Table III includes the center of the PFA sample after aging, where the central surface exhibits less erosion compared to the FEP sample. Additionally, small spots resembling crystals were observed and analyzed with Raman spectroscopy.

TABLE II
MEAN SURFACE ROUGHNESS (S_a) MEASURED ON AGED SAMPLES FROM POS. 1 TO 3 WRT. FIG. 4. UNITS IN NM.

Position	XLPE	FEP	PFA
1	3251	1199	534
2	957	147	334
3[*]	357	203	503

[*] Equivalent to an unaged sample/reference.

TABLE III
SURFACE CHARACTERIZATION RESULTS OBTAINED USING PROFILOMETER, MICROSCOPE, FTIR, AND RAMAN SPECTROSCOPY.
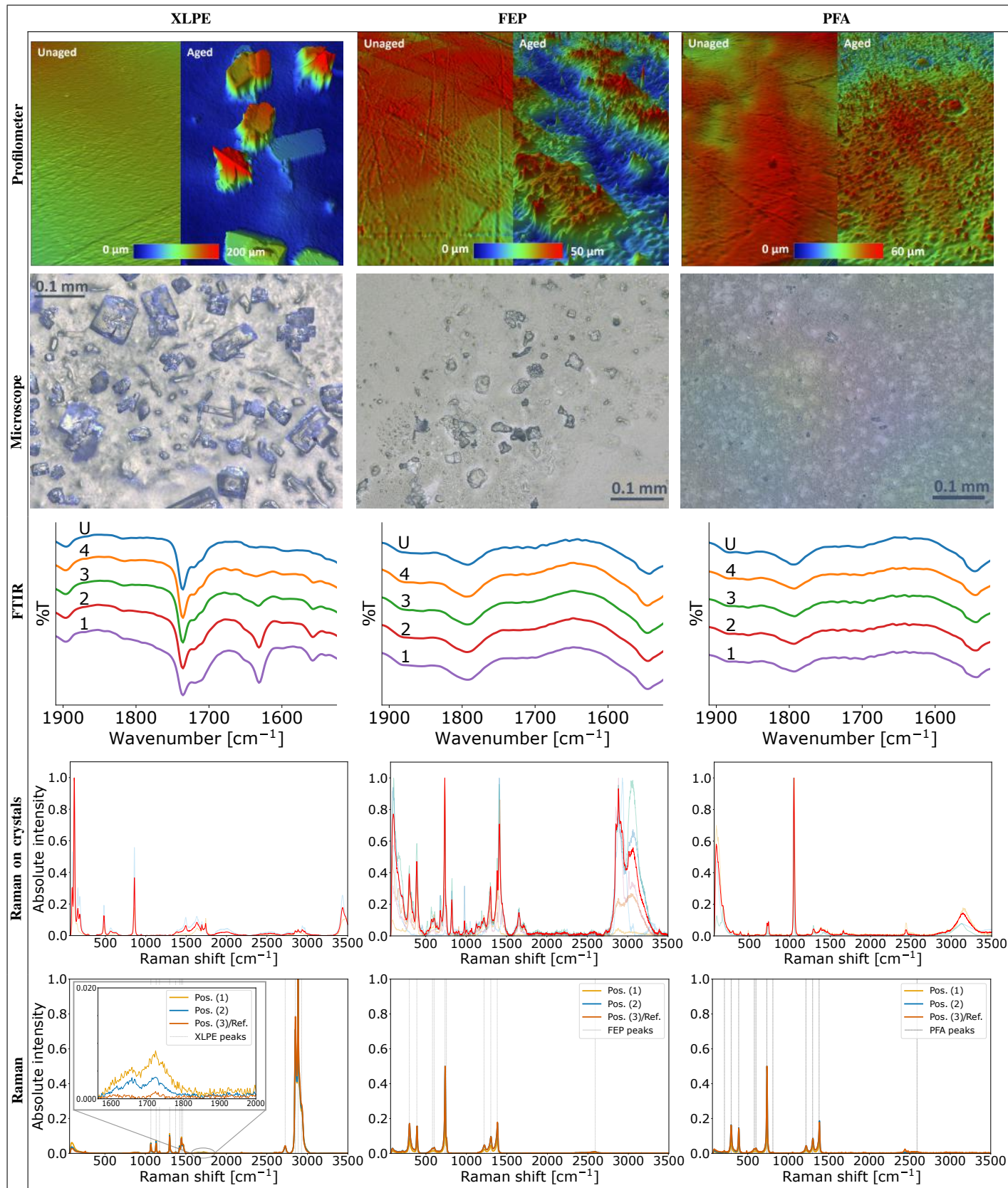
2) FTIR: The row labeled 'FTIR' in Table III presents the FTIR results from the center of each aged sample (Pos. 1). It includes a plot from an unaged sample (U) alongside plots that represent different depths into the bulk of the aged samples, with depth levels ranging from 1 to 4, with 4 being the deepest point, as displayed in Fig. 4. For the XLPE samples, there is an observed increase in absorption at several wavelengths from the deepest point (4) towards the sample surface (1), where slice 4 showed the most similarity to the unaged surface (U). In contrast, the fluoropolymers (FEP and PFA) exhibit no significant differences in absorption across these wavelengths. Samples from Pos. 3 showed identical results to that of an unaged sample; therefore, they can also be regarded as a reference.

Fig. 12a shows the FTIR spectra of XLPE from the aged center (Pos. 1) and an unaged sample for the carbonyl region. The aged sample shows increased absorption in this region compared to the unaged sample, and several new peaks can be identified in the spectrum. The absorption at these peaks decreases with the distance from the center and with the depth into the bulk. A new peak appeared at 1276 cm^{-1}. There was also slightly more absorption between 3500 cm^{-1} and 3000 cm^{-1} for the aged sample. The strong transmittance likely caused the truncation of the signals. The significant differences in absorbances and the appearance of new peaks indicate the presence of oxalic acid (crystals) or similar by-products on the surface, as depicted in Stage 3 of Fig. 1.

In the FTIR spectroscopic analysis, the comparison between unaged and aged FEP and PFA samples (Pos. 1) revealed no significant spectral changes. Therefore, Fig. 12b presents the spectra obtained only from the aged samples.
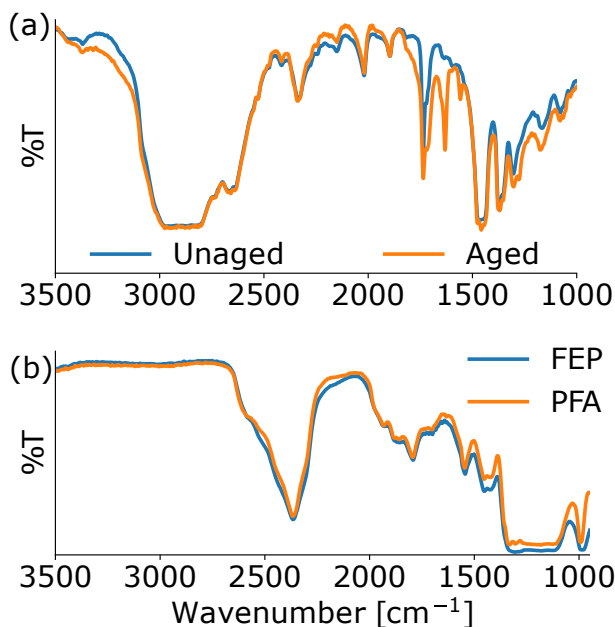

Fig. 12. FTIR results for (a) Unaged and aged XLPE samples. (b) Aged FEP and PFA samples. No significant differences were observed between unaged and aged FEP and PFA.

3) Raman Spectroscopy and Microscope: We analyzed unaged and aged samples through Raman spectroscopy and light microscopy, with representative images presented in Table III.

Analyses for Raman spectroscopy were performed using the punched-out samples from the specified positions (Pos. 1–3) from the top and bottom samples, as illustrated in Fig. 4. The results from Pos. 3 were analogous to an unaged sample; thus, the Pos. 3 samples can be considered as references. In Table III, the row labeled 'Raman on crystals' specifically focuses on the crystal-like artifacts found in aged areas. Red waveforms indicate the average outcomes of six measurements, with each measurement displayed as a faint color in the background.

The sample's surface appeared significantly grainy around the cavity area, as shown in Fig. 10. The roughness of the surface can be attributed to the impact of charged particle bombardment, as discussed in Section IV-B. Observations of an aged XLPE sample from Pos. 1 revealed diverse crystal formations in terms of shape and size (30–150 μm) as can be seen in the 'Microscope' row of Table III). Raman analysis identified these crystals as hydrated oxalic acid ($C_2H_2O_4 \cdot 2H_2O$), with peaks at 478, 560, 855, 1490, 1628, 1728, and 3440 cm^{-1} ('Raman on crystals' row in Table III), corroborating with findings from [28]. Additionally, the portions of the aged and eroded surface free of crystals (Pos. 1) were scrutinized using Raman spectroscopy. Comparisons of samples from Pos. 2 and 3 and an unaged sample revealed no formation of new chemical bonds, as can be seen in the 'Raman' row of Table III), suggesting that the surface modifications outside the cavity area, if any, were predominantly physical rather than chemical.

On the spectra of the XLPE sample, a new peak around 1720 cm^{-1} was observed in the case of samples taken from Pos. 1 (aged) and Pos. 2 (close to the cavity wall) with it being more prominent for the aged sample (shown in the inlet of the Raman figure in Table III). It signifies the presence of C=O bond (carbonyl group), reminiscent of oxidation [47], [48]. The FTIR results for XLPE, as displayed in Fig. 12a and Table III, also reveal pronounced carbonyl absorption around 1720 cm^{-1}, indicative of an increased level of oxidation. This observation is consistent with findings reported in [49].

In the case of FEP samples, the aged cavity area also displayed evident signs of erosion and melted patches containing crystals. Compared to the XLPE samples, both the number of crystals and the extent of erosion in the FEP samples were considerably less, as demonstrated by the microscope images in Table III. These crystals were measured to be approximately 40–80 μm in diameter. The Raman spectra taken from Pos. 1–3 on these samples indicated notable differences. Specifically, distinct peaks associated with C−H bonds were identified at 1063, 1129, 1416, 1440, 1463, 2885, 2848, and 2930 cm^{-1} in the crystals present on the surface, as exhibited in Table III. Conversely, Raman analysis at Pos. 1 on areas without visible crystals revealed no significant spectral deviations compared to Pos. 2 and 3.

The microscope images of PFA samples showed similar surface degradation as the FEP samples, with defined melted bumps and eroded surface in the cavity area (Table III). The aged cavity area displayed much fewer and smaller crystals compared to the XLPE and FEP samples (Table III). The Raman spectra of these crystals showed C−H bond vibrations around 1063, 1129, 1416, 1440, 1463, 2885, 2848, 2930 cm^{-1}.

Similar to XLPE and FEP, Raman analysis of PFA surface sections without crystals (Pos. 1) showed no deviation from Pos. 2 and 3, as shown in Table III.

Besides profilometry and microscopy, Raman and FTIR analyses indicated that XLPE samples underwent significant aging, characterized by oxidation and chemical changes that extend from the surface to the bulk of the material. Conversely, PD-aged FEP and PFA samples showed consistent chemical stability, with peak patterns matching those of unaged samples, indicating fluoropolymers' higher resistance to electrical PD aging than XLPE. These findings closely match the aging mechanisms discussed in Section IV-B.

V. CONCLUSION

This study, investigating the effects of PD-induced aging on fluoropolymer insulation materials, with a particular focus on FEP and PFA compared to XLPE as the reference, has revealed that FEP and PFA exhibit superior durability under identical electrical discharge conditions. Throughout the three-week aging process until the last few hours, the main body of the PRPD data for FEP and PFA remained relatively stable, suggesting minimal alterations in surface chemistry and roughness. In the last few hours, however, there was a shift from turtle-like to rabbit-like patterns in PRPDs for FEP and PFA, hinting that surface conductivity started to increase. Conversely, for XLPE, reductions in both the number of discharges and width of PD clusters were observed within the first few hours, indicating a rapid rise in the surface conductivity, which resulted in significant erosion and crystal formation over the extended duration of the experiment.

Microscopic and profilometric analyses showed that FEP and PFA surfaces underwent fewer PD-induced changes, as indicated by a lower concentration of degradation by-products, such as crystal-like structures. On the other hand, XLPE surfaces suffered significant pitting and erosion and exhibited widespread crystal formations. The FTIR and Raman spectroscopy results underlined the chemical robustness of FEP and PFA, likely due to their carbon-fluorine bonds, which resulted in reduced material degradation and by-product formation compared to XLPE.

The PD aging process, characterized by the development of specific PD patterns and alterations in surface roughness and chemical composition, indicated a gradual aging effect on the electrical insulating properties of fluoropolymers. Unlike XLPE, which suggested significant erosion after just a few hours of PD exposure, FEP and PFA only signaled an increase in surface conductivity after 500 hours of exposure. In conclusion, this study contributes to a better understanding of the electrical aging behaviors of fluoropolymer insulation materials in high-voltage cables. Future research will delve into high-temperature PD aging and degradation mechanisms, including more extended aging durations.

REFERENCES

[1] P. Yang, K. Tian, X. Ren, and K. Zhou, "A comparative study of electrical aging of multiwalled carbon nanotubes and carbon black filled cross-linked polyethylene," *Nanocomposites*, vol. 5, no. 4, pp. 95–103, 2019.

[2] C. Blivet, J.-F. Larché, Y. Israëli, P.-O. Bussière, and J.-L. Gardette, "Thermal oxidation of cross-linked PE and EPR used as insulation materials: Multi-scale correlation over a wide range of temperatures," *Polymer Testing*, vol. 93, p. 106913, Jan. 2021. [Online]. Available: https://linkinghub.elsevier.com/retrieve/pii/S0142941820321425

[3] D. W. Brown and L. A. Wall, "High-temperature aging of fluoropolymers," *Journal of Polymer Science Part A-1: Polymer Chemistry*, vol. 10, no. 10, pp. 2967–2982, 1972.

[4] R. Zhou, S. Fu, H. Jiang, X. Li, and G. Zhou, "Thermal accelerated aging study of water/fluoropolymer/ito contact in electrowetting display systems," *Results in Physics*, vol. 15, p. 102737, 2019.

[5] M. P. Bracciale, L. Capasso, F. Sarasini, J. Tirillò, and M. L. Santarelli, "Effect of aging on the mechanical properties of highly transparent fluoropolymers for the conservation of archaeological sites," *Polymers*, vol. 14, no. 5, p. 912, 2022.

[6] C. Fu, X. Qiu, A. Gu, and Z. Yu, "Stabilization of perfluorinated ethylene-propylene by esterification with short-chain alcohols," *Materials Research Express*, vol. 5, no. 6, p. 065314, 2018.

[7] T. Paulmier, R. Hanna, M. Belhaj, B. Dirassen, D. Payan, N. Balcon, C. Tonon, E. Dantras, and A. Bernès, "Aging effect and induced electric phenomena on dielectric materials irradiated with high energy electrons," *IEEE Transactions on Plasma Science*, vol. 41, no. 12, pp. 3422–3428, 2013.

[8] J. Densley, "Ageing mechanisms and diagnostics for power cables - an overview," *IEEE Electrical Insulation Magazine*, vol. 17, no. 1, pp. 14–22, Jan. 2001. [Online]. Available: http://ieeexplore.ieee.org/document/901613/

[9] T. Shahsavarian, Y. Pan, Z. Zhang, C. Pan, H. Naderiallaf, J. Guo, C. Li, and Y. Cao, "A Review of Knowledge-Based Defect Identification via PRPD Patterns in High Voltage Apparatus," *IEEE Access*, vol. 9, pp. 77 705–77 728, 2021.

[10] G. Lopez, "High-Performance Polymers for Aeronautic Wires Insulation: Current Uses and Future Prospects," *Recent Progress in Materials*, vol. 3, no. 1, pp. 1–15, Feb. 2021. [Online]. Available: https://www.lidsen.com/journals/rpm/rpm-03-01-005

[11] D. America. PFA - Daikin America. Accessed: 2023-10-24. [Online]. Available: https://daikin-america.com/pfa-fluoropolymers/

[12] Zeus Industrial Products, Inc. (2019, Feb 20) Understanding fluoropolymers. Accessed on: 2023-10-22. [Online]. Available: https://www.azom.com/article.aspx?ArticleID=17673

[13] C. A. Orme, E. J. Cho, and J. Lewicki, "Fluoropolymer Aging Assessments," Lawrence Livermore National Lab. (LLNL), Livermore, CA (United States), Tech. Rep. LLNL-TR-827066, Sep. 2021. [Online]. Available: https://www.osti.gov/biblio/1822604

[14] M. A. Baferani, C. Li, T. Shahsavarian, J. Ronzello, and Y. Cao, "High Temperature Insulation Materials for DC Cable Insulation — Part I: Space Charge and Conduction," *IEEE Transactions on Dielectrics and Electrical Insulation*, vol. 28, no. 1, pp. 223–230, Feb. 2021. [Online]. Available: https://ieeexplore.ieee.org/document/9351872/

[15] T. Shahsavarian, C. Li, M. A. Baferani, J. Ronzello, Y. Cao, X. Wu, and D. Zhang, "High Temperature Insulation Materials for DC Cable Insulation—Part II: Partial Discharge Behavior at Elevated Altitudes," *IEEE Transactions on Dielectrics and Electrical Insulation*, vol. 28, no. 1, pp. 231–239, Feb. 2021. [Online]. Available: https://ieeexplore.ieee.org/document/9351868/

[16] C. Li, T. Shahsavarian, M. A. Baferani, N. Wang, J. Ronzello, and Y. Cao, "High Temperature Insulation Materials for DC Cable Insulation — Part III: Degradation and Surface Breakdown," *IEEE Transactions on Dielectrics and Electrical Insulation*, vol. 28, no. 1, pp. 240–247, Feb. 2021. [Online]. Available: https://ieeexplore.ieee.org/document/9351846/

[17] P. Morshuis, "Degradation of solid dielectrics due to internal partial discharge: some thoughts on progress made and where to go now," *IEEE Transactions on Dielectrics and Electrical Insulation*, vol. 12, no. 5, pp. 905–913, Oct. 2005.

[18] K. Temmen, "Evaluation of surface changes in flat cavities due to ageing by means of phase-angle resolved partial discharge measurement," *Journal of Physics D: Applied Physics*, vol. 33, no. 6, pp. 603–608, Mar. 2000. [Online]. Available: https://doi.org/10.1088/0022-3727/33/6/303

[19] P. H. F. Morshuis, "Partial discharge mechanisms," Ph.D. dissertation, Delft University of Technology, 1993.

[20] C. Hudon, R. Bartnikas, and M. Wertheimer, "Surface conductivity of epoxy specimens subjected to partial discharges," in *IEEE International Symposium on Electrical Insulation*, Jun. 1990, pp. 153–155, iSSN: 1089-084X.

[21] L. A. Dissado and J. C. Fothergill, *Electrical Degradation and Breakdown in Polymers*. IET, 1992.

[22] K. C. Kao, *Dielectric Phenomena in Solids*. Elsevier, May 2004.

[23] "FEP vs. PFA :: MakeItFrom.com." [Online]. Available: https://www.makeitfrom.com/compare/Fluorinated-Ethylene-Propylene-FEP/Perfluoroalkoxy-PFA

[24] H. Teng, "Overview of the Development of the Fluoropolymer Industry," *Applied Sciences*, vol. 2, no. 2, pp. 496–512, Jun. 2012. [Online]. Available: https://www.mdpi.com/2076-3417/2/2/496

[25] P. G. Kelleher, "Thermal oxidation of thermoplastics," *Journal of Applied Polymer Science*, vol. 10, no. 6, pp. 843–857, 1966. [Online]. Available: https://onlinelibrary.wiley.com/doi/abs/10.1002/app.1966.070100602

[26] U. H. Hossain, F. Muench, and W. Ensinger, "A comparative study on degradation characteristics of fluoropolymers irradiated by high energy heavy ions," *RSC Advances*, vol. 4, no. 91, pp. 50 171–50 179, Oct. 2014, publisher: The Royal Society of Chemistry. [Online]. Available: https://pubs.rsc.org/en/content/articlelanding/2014/ra/c4ra04635h

[27] L. Wang, A. Cavallini, G. C. Montanari, and L. Testa, "Evolution of pd patterns in polyethylene insulation cavities under AC voltage," *IEEE Transactions on Dielectrics and Electrical Insulation*, vol. 19, no. 2, pp. 533–542, Apr. 2012.

[28] C. Hudon, R. Bartnikas, and M. Wertheimer, "Analysis of degradation products on epoxy surfaces subjected to pulse and glow type discharges," in *1991 Annual Report. Conference on Electrical Insulation and Dielectric Phenomena,*, Oct. 1991, pp. 237–243. [Online]. Available: https://ieeexplore.ieee.org/abstract/document/763364

[29] PlasticsEurope, *Guide for the Safe Handling of Fluoropolymer Resins*, PlasticsEurope.

[30] BÖHLER. L276 Product Description. Accessed: 2023-11-09. [Online]. Available: https://www.bohler-edelstahl.com/en/products/l276/

[31] I. Gallimberti, "The mechanism of the long spark formation," *Le Journal de Physique Colloques*, vol. 40, no. C7, pp. C7–250, Jul. 1979. [Online]. Available: http://dx.doi.org/10.1051/jphyscol:19797440

[32] T. G. Aakre, E. Ildstad, and S. Hvidsten, "Partial discharge inception voltage of voids enclosed in epoxy/mica versus voltage frequency and temperature," *IEEE Transactions on Dielectrics and Electrical Insulation*, vol. 27, no. 1, pp. 214–221, Feb. 2020. [Online]. Available: https://ieeexplore.ieee.org/document/8985636

[33] H. Illias, T. S. Yuan, A. H. A. Bakar, H. Mokhlis, G. Chen, and P. L. Lewin, "Partial discharge patterns in high voltage insulation," in *2012 IEEE International Conference on Power and Energy (PECon)*, Dec. 2012, pp. 750–755.

[34] T. Shahsavarian and S. M. Shahrtash, "Modelling of aged cavities for partial discharge in power cable insulation," *IET Science, Measurement & Technology*, vol. 9, no. 6, pp. 661–670, 2015. [Online]. Available: https://onlinelibrary.wiley.com/doi/abs/10.1049/iet-smt.2014.0222

[35] P. H. F. Morshuis and F. H. Kreuger, "Transition from streamer to Townsend mechanisms in dielectric voids," *Journal of Physics D: Applied Physics*, vol. 23, no. 12, pp. 1562–1568, Dec. 1990. [Online]. Available: https://doi.org/10.1088/0022-3727/23/12/012

[36] P. H. F. Morshuis, "Partial discharge mechanisms in voids related to dielectric degradation," *IEE Proceedings - Science, Measurement and Technology*, vol. 142, no. 1, pp. 62–68, Jan. 1995. [Online]. Available: https://digital-library.theiet.org/content/journals/10.1049/ip-smt_19951562

[37] ——, "Partial discharge mechanisms: Mechanisms leading to breakdown, analyzed by fast electrical and optical measurements," Ph.D. dissertation, TU Delft, 1993. [Online]. Available: https://repository.tudelft.nl/islandora/object/uuid%3A5e39ece9-bcb1-40e0-8501-cfb963873a78

[38] C.-S. Kim, T. Kondo, and T. Mizutani, "Change in PD pattern with aging," *IEEE Transactions on Dielectrics and Electrical Insulation*, vol. 11, no. 1, pp. 13–18, Feb. 2004. [Online]. Available: https://ieeexplore.ieee.org/abstract/document/1266311

[39] Y. Sekii and K. Yamauchi, "Analysis of deterioration by partial discharge of XLPE using GCMS and FTIR," in *2008 International Conference on Condition Monitoring and Diagnosis*, Apr. 2008, pp. 251–254. [Online]. Available: https://ieeexplore.ieee.org/abstract/document/4580274

[40] C. Pan, K. Wu, G. Chen, Y. Gao, M. Florkowski, Z. Lv, and J. Tang, "Understanding Partial Discharge Behavior from the Memory Effect Induced by Residual Charges: A Review," *IEEE Transactions on Dielectrics and Electrical Insulation*, vol. 27, no. 6, pp. 1951–1965, Dec. 2020. [Online]. Available: https://ieeexplore.ieee.org/document/9293218/

[41] F. Gutfleisch and L. Niemeyer, "Measurement and simulation of PD in epoxy voids," *IEEE Transactions on Dielectrics and Electrical Insulation*, vol. 2, no. 5, pp. 729–743, Oct. 1995. [Online]. Available: https://ieeexplore.ieee.org/abstract/document/469970

[42] K. Wu, T. Ijichi, T. Kato, Y. Suzuoki, F. Komori, and T. Okamoto, "Contribution of surface conductivity to the current forms of partial discharges in voids," *IEEE Transactions on Dielectrics and Electrical Insulation*, vol. 12, no. 6, pp. 1116–1124, Dec. 2005. [Online]. Available: https://ieeexplore.ieee.org/abstract/document/1561791

[43] C. Forssen and H. Edin, "Partial discharges in a cavity at variable applied frequency part 1: measurements," *IEEE Transactions on Dielectrics and Electrical Insulation*, vol. 15, no. 6, pp. 1601–1609, Dec. 2008.

[44] Z. Lei, J. Song, M. Tian, X. Cui, C. Li, and M. Wen, "Partial discharges of cavities in ethylene propylene rubber insulation," *IEEE Transactions on Dielectrics and Electrical Insulation*, vol. 21, no. 4, pp. 1647–1659, Aug. 2014.

[45] C. Hudon, R. Bartnikas, and M. R. Wertheimer, "Chemical and physical degradation effects on epoxy surfaces exposed to partial discharges," in *Proceedings of 1994 4th International Conference on Properties and Applications of Dielectric Materials (ICPADM)*, vol. 2. IEEE, 1994.

[46] T. Tanaka, "Internal Partial Discharge and Material Degradation," *IEEE Transactions on Electrical Insulation*, vol. EI-21, no. 6, pp. 899–905, Dec. 1986. [Online]. Available: https://ieeexplore.ieee.org/abstract/document/4157085

[47] A. P. Kotula, C. R. Snyder, and K. B. Migler, "Determining conformational order and crystallinity in polycaprolactone via raman spectroscopy," *Polymer*, vol. 117, pp. 1–10, 2017.

[48] G. Socrates, *Infrared and Raman characteristic group frequencies: tables and charts*. John Wiley & Sons, 2004.

[49] S. Hvidsten, R. Floden, K. Olafsen, and L. Lundegaard, "Long term electrical properties of XLPE cable insulation system for subsea applications at very high temperatures," in *CEIDP '05. 2005 Annual Report Conference on Electrical Insulation and Dielectric Phenomena, 2005.*, Oct. 2005, pp. 265–268, iSSN: 0084-9162.

Emre Kantar received the B.Sc. and M.Sc. degrees in Electrical and Electronics Engineering from the Middle East Technical University (METU), Ankara, in 2011 and 2014, respectively. He received his Ph.D. in Electric Power Engineering from the Norwegian University of Science and Technology (NTNU), Trondheim in 2019. Since 2018, he has been working as a research scientist at SINTEF Energy Research, Trondheim, Norway. His main research interests include pre-breakdown and breakdown phenomena in solid insulating materials.

Katharina Kuhlefelt Eie-Klusmeier received her M.Sc degree in applied physics from the Norwegian University of Science and Technology (NTNU), Trondheim, Norway, in 2022. Since 2022, she has been working at the Department of Electric Power Technology at SINTEF Energy Research. Her research work has mainly focused on the degradation of electric insulation materials and material characterization techniques (e.g. FTIR and DSC).

Marit-Helen Glomm Ese received the Ph.D. degree in surface- and colloid chemistry from the University of Bergen in 1999. After several engagements as a postdoc and research scientist both in the USA (North Carolina State University) and Norway (Norwegian University of Science and Technology), she joined SINTEF Energy Research in 2006. She is working on material science for electric power apparatus. Her main focus has been on the aging and degradation of different insulating materials (polymers, liquids, and paper).

Torbjørn Andersen Ve was born in Bergen, Norway, in 1983. He received the M.Sc. degree in physics and the Ph.D. degree in electric power engineering from the Norwegian University of Science and Technology (NTNU), Trondheim, Norway, in 2008 and 2021, respectively. He joined SINTEF Energy Research, Trondheim, in 2008, where he is currently a Research Scientist, working on topics such as charge accumulation and transport in solid insulation materials, liquid and gas absorption in polymer materials, and electrical aging phenomena in polymer insulation.

Sverre Hvidsten received the M.Sc. degree from the Norwegian Institute of Technology (NTH), Trondheim, Norway, in 1992, and the Ph.D. degree in electrical engineering from the Norwegian University of Science and Technology (NTNU), Trondheim, in 1999. From 1993 to 1994, he was a Researcher with Electricity Supply Research Institute (EFI), Norway. He then joined SINTEF Energy Research, Trondheim, where he is currently a Senior Researcher. He also participates in International Council on Large Electric Systems (CIGRE) work.